Three-dimensional mapping and regulation of action potential propagation in nanoelectronics innervated tissues

HHS Public Access

Author manuscript

Nat Nanotechnol. Author manuscript; available in PMC 2017 March 01.

Published in final edited form as:

Nat Nanotechnol. 2016 September ; 11(9): 776–782. doi:10.1038/nnano.2016.96.

Three-dimensional mapping and regulation of action potential propagation in nanoelectronics innervated tissues

Xiaochuan Dai[1,*], **Wei Zhou**[1,*], **Teng Gao**[1], **Jia Liu**[1], and **Charles M. Lieber**[1,2]

[1]Department of Chemistry and Chemical Biology, Harvard University, Cambridge, Massachusetts 02138, USA

[2]Harvard John A. Paulson School of Engineering and Applied Sciences, Harvard University, Cambridge, Massachusetts 02138, USA

Abstract

Real-time mapping and manipulation of electrophysiology in three-dimensional (3D) tissues could impact broadly fundamental scientific and clinical studies, yet realization lacks effective methods. Here we introduce tissue-scaffold-mimicking 3D nanoelectronic arrays consisting of 64 addressable devices with subcellular dimensions and sub-millisecond time-resolution. Real-time extracellular action potential (AP) recordings reveal quantitative maps of AP propagation in 3D cardiac tissues, enable *in situ* tracing of the evolving topology of 3D conducting pathways in developing cardiac tissues, and probe the dynamics of AP conduction characteristics in a transient arrhythmia disease model and subsequent tissue self-adaptation. We further demonstrate simultaneous multi-site stimulation and mapping to manipulate actively the frequency and direction of AP propagation. These results establish new methodologies for 3D spatiotemporal tissue recording and control, and demonstrate the potential to impact regenerative medicine, pharmacology and electronic therapeutics.

Developments in cardiac tissue engineering over the past two decades[1–5] have substantially advanced *in vitro* models for drug-screening[6–8] and disease studies[9], as well as *in vivo* implants to replace diseased or damaged tissues[10, 11], for example, resulting from myocardial infarction[11]. However, effective methodologies for real-time 3D mapping and manipulation of electrical activity in studies of tissue development, drug modulation and implantation have thus far been missing. Optical imaging using exogenous or genetically-encoded voltage-sensitive dyes[12–14] has allowed high spatial-resolution mapping of AP

Correspondence and requests for materials should be addressed to: C.M.L. (cml@cmliris.harvard.edu).

*These authors contributed equally to this work.

Author contributions

X. D., W. Z. and C. M. L. conceived and designed the experiments. X. D., W. Z., T. G. and J. L. performed the experiments and analyzed the data. X. D., W. Z. and C. M. L. co-wrote the paper. All authors discussed the results and commented on the manuscript.

Competing financial interests

The authors declare no competing financial interests.

Supplementary information accompanies this paper at www.nature.com/naturenanotechnology.

propagation but can be limited by a relatively slow time-resolution in 3D scanning[13–15] and light scattering in tissues[13, 15]. On the other hand, multiplexed electrical recordings with planar microelectrodes[8, 16] or field-effect transistor (FET)[17, 18] arrays can map APs with a sub-millisecond temporal resolution, but have been limited to studies of 2D cultured cells[17] or the surfaces of 3D tissue samples[18].

To overcome the key gaps in existing optical voltage sensing and planar electrode device methods, we previously introduced a 3D nanoelectronics scaffold concept that could access cellular response from within engineered tissues[19], although the size and mechanical mismatches precluded 3D tissue mapping. Here we present a new class of tissue-scaffold-mimicking nanoelectronics designed with both dimensions and mechanical properties comparable to the conventional cardiac tissue scaffold poly(lactic-co-glycolic acid) (PLGA) electro-spun fibers[2, 4, 20] (Supplementary Information). These new nanoelectronics have been used as cardiac tissue scaffolds alone or together with PLGA auxiliary layers to enable real-time mapping of APs across 3D samples with sub-millisecond temporal resolution. In addition, incorporation of stimulator electrodes allows for simultaneous active control and mapping of cardiac tissue electrophysiology in 3D.

3D Activity Mapping from Nanoelectronics-Cardiac Tissues

The 3D nanoelectronics-cardiac tissues were prepared using a strategy that involves three major steps (Figs. 1a–c). First, 350–750-nm-thick 2D polymeric meshes with embedded nanoelectronics are fabricated on a substrate by photolithography on a Ni release layer with free-standing structures achieved following Ni etching. To meet the feature size and mechanical property criteria for tissue-scaffold-like nanoelectronics, we used high-density silicon nanowire assembly to obtain a >95% yield of 1–2 μm footprint free-standing FET arrays (Supplementary Information, Fig. 1a and Supplementary Fig. 4a). Significantly, this new design has stiffness values of SU-8/metal/SU-8 and SU-8 elements, 2.8×10^{-16} and 2.9×10^{-17} N m^2, respectively, comparable to 1 μm diameter PLGA electro-spun fibers, 1.0×10^{-16} N m^2, used as cardiac tissue scaffolds[2, 4, 20] (Supplementary Information); that is, the free-standing nanoelectronics are tissue scaffold-like in terms of mechanical properties.

The 2D free-standing meshes were folded into 3D nanoelectronic scaffolds (Fig. 1b; Supplementary Figs. 4b–f), and then neonatal rat ventricular cells were seeded and cultured to yield nanoelectronics-cardiac tissue (Fig. 1c; Supplementary Information). While these studies focus on ca. planar structures typical for engineered cardiac tissue patches[3, 7, 19], nanoelectronic scaffolds could also be folded over curved structures to yield nonplanar structures or rolled into cylinders. Representative confocal microscopy images taken at 7 days *in vitro* (DIV; Supplementary Fig. 6) show characteristic adult sarcomere lengths of 2.1 ± 0.1 μm[21] with alignment to the scaffold. Extracellular cardiac AP signals recorded from 4 × 4 FET sensors in a single layer across 5 × 5 mm^2 domain (Fig. 1d) show a synchronized beating rate of 1.8 Hz, amplitude of 1–2 mV and peak width of ca. 1 ms from all 16 channels, consistent with extracellular recording results of FET devices on planar chips[17]. Higher resolution examination of these peaks (Fig. 1e) reveals sub-millisecond time latency between any given set of AP peaks recorded by the 16 FET sensors, where the intrinsic

device time-resolution is 0.01–0.05 ms (Supplementary Information), substantially better than the time-scale of observed AP peak or peak latency.

To better visualize the AP propagation, we plot these data from the single layer as an isochronal map of time latency (Fig. 1f). This map, which covers 5 × 5 mm^2 area of tissue, shows that the AP wavefront propagates from FET(x,y = 4,1) to FET(1,4). Combining the spatiotemporal AP recording results from all the 64 FET sensors designed in four layers, we plot a 3D isochronal map of time latency (Fig. 1g) that visualizes the 3D waveform of AP conduction in the nanoelectronics-cardiac tissue. The similarity but not identical latency between z-coordinates is consistent with the small (50 μm) distance between neighboring nanoelectronic mesh layers, and also highlights the well-developed 3D coherence of the cellular networks. Further evidence to this latter point is that the average conduction velocity, 28 ± 2 cm/s, is very similar with that of *in vivo* neonatal rat heart tissue, 21–27 cm/s[5].

3D Activity Mapping During Cardiac Tissue Development

We have investigated the evolution of electrophysiological activity during culture and tissue development using nanoelectronics-cardiac tissues. 3D real-time mapping of APs carried out at 2, 4, 6 and 8 DIV from a 6 × 4 × 2 array of integrated FETs (Fig. 2a), highlights several key points. Qualitatively, analyses of recorded AP maps show that the spontaneous beating volume expands to the entire sample for ≥6 DIV. Second, quantitative analyses of these data show that percentage volume of detectable activity at 2, 4, 6 and 8 DIV are ca. 46, 79, 98 and 98%, respectively. Third, examination of real-time AP data recorded at 2 DIV where the spontaneous beating tissue regions are sparse (Supplementary Fig. 8) demonstrates that beating is synchronized within and between different device layers. These latter results suggest that the 3D topology of the conducting pathways develop early during engineered cardiac tissue maturation. More generally, while progress has been made on 3D structural visualization of cardiac tissue development[22], it is still difficult to map directly 3D functional networking during tissue maturation, and thus the nanoelectronics-cardiac tissue provides a complementary method to address this key issue.

In addition, analysis of the AP data further demonstrates that at 2, 4, 6 and 8 DIV, the beating rate values (Supplementary Fig. 9) are 346, 470, 52 and 38 per minute, respectively. The beating rate shows a substantial decrease after 4 DIV, as expected during maturation of rat cardiac tissue[23, 24]. The average extracellular AP amplitude from the samples at 2, 4, 6 and 8 DIV (Fig. 2b), 1.27 ± 42%, 1.77 ± 49%, 1.92 ± 34% and 1.27 ± 32% mV, respectively, also exhibit averaged amplitude variations, although the values are statistically overlapping. We do note that the smallest coefficient of variation (± 32%) occurs at 8 DIV suggesting an increase in uniformity of amplitudes and cell growth on the scaffolds along with tissue development, since the extracellular AP amplitudes are affected by factors such as the cell-to-device distance and sealing[25]. These results show that nanoelectronics-cardiac tissue can provide insight into the electrophysiological development in 3D, and thus could impact research in cardiac tissue engineering and regeneration, including stem cell differentiation, growth factors and ischemia[26, 27].

3D Monitoring of Cardiac Pharmacological and Disease Models

We have used nanoelectronics-cardiac tissue to investigate responses to drugs (Fig. 3; Supplementary Figs. 10 and 11; Supplementary Information), with a focus on the 3D dynamics and AP propagation in a drug-induced ventricular arrhythmia model[28]. β-Adrenergic receptor agonists such as norepinephrine are used to treat heart failure, but during local injection can produce ventricular arrhythmia and sudden cardiac death[28]. We investigate this phenomenon by focal injection of norepinephrine on 3D nanoelectronics-cardiac tissues (Fig. 3a) while simultaneously recording real-time 3D APs. Representative data from three FET sensors in different layers before and following norepinephrine injection near sensor *L1*(4,3) (Figs. 3b–c) highlight dynamic instability of the conduction pathway. Examination of time-correlated AP peaks from these three devices before and 5–10 s post-injection (Fig. 3c) shows that the AP propagates initially from sensor *L3*(4,1) to *L1*(4,3), but that ca. 10 s after drug injection the propagation direction is reversed. In the intermediate regime, the recorded peaks indicate an earlier depolarization around sensor *L1*(4,3), which then leads to the reversal of the overall propagation direction. At steady-state post-injection, the full 3D AP isochronal maps (Fig. 3d) show clearly that a new stable 3D AP propagation direction arising from the norepinephrine injection location has overridden the original pace-maker foci.

In contrast, independent experiments with homogeneous perfusion of norepinephrine (Supplementary Fig. 10) and 1-heptanol (Supplementary Fig. 11) serve both as controls and highlight additional capabilities of the nanoelectronics-cardiac tissue for pharmacological assays. Homogeneous norepinephrine perfusion yields a 150% increase in beating rate at steady-state, and importantly, measurements (Supplementary Fig. 10b) demonstrated full 3D synchronization of APs from sensors in different regions of the tissue, in contrast to focal injection (Fig. 3). Interestingly, the high temporal resolution 3D mapping exhibited a transient conduction velocity increase over the initial 60 s of perfusion (17% peak increase ca. 30 s after start). Perfusion of the gap-junction blocker[8] 1-heptanol, which inhibits cell-to-cell current conduction via intercellular gap-junctions, results in a uniform decrease in AP conduction velocity/increase in latency (Supplementary Figs. 11b–c). High temporal resolution characterization of the AP conduction velocity at the single peak level without averaging allows monitoring diffusion and action of 1-heptanol from the top surface through the interior of the tissue in real-time. These temporally- and spatially-varying effects, including the dynamic instability associated with non-uniform norepinephrine addition (Fig. 3), would otherwise have been difficult to detect using methods that require averaging of AP peaks and/or scanning in order to resolve accurate time latency in 3D.

Simultaneous Mapping and Manipulation of Cardiac Activity

Beyond real-time mapping of propagating APs, incorporation of stimulators could open up the capability for simultaneous manipulation of the tissue electrophysiology as required for closed-loop control of cardiac activity and/or to treat abnormalities. To this end, we incorporated individually addressable electrical stimulators together with nanowire FET sensors into nanoelectronics scaffolds (Fig. 4a; Supplementary Information). As an illustration, application of a variable amplitude 1.25 Hz stimulation spike train to one of the

stimulators in the nanoelectronics-cardiac tissue (Fig. 4b and Supplementary Fig. 12) yields AP peaks recorded in different regions (*L1–L3*) of the tissue locked to the stimulation frequency when the stimulator pulse amplitude is 1 V; and for amplitudes ≤100 mV the natural ca. 1 Hz beating frequency of the tissue is observed (Supplementary Fig. 12). Interestingly, the coefficient of variation of the beating rate increases by 4.3× (from 2.7% to 11.7%) as the stimulation amplitude increases from 1 to 100 mV (Supplementary Fig. 12f), suggesting a dynamic instability of cardiomyocytes prior to the locking to the pacing rate. Further studies of stimulation at 1 V versus frequency (Supplementary Fig. 13) show stable locking of the tissue beating for 1.25, 1.67 and 2.5 Hz stimulation, and thus, suggest the potential to modulate cardiac activity on demand.

Last, we use the active stimulation and monitoring capabilities to illustrate spatial manipulation of AP propagation direction within tissues. Specifically, a nanoelectronics-cardiac tissue sample with original pace-maker foci located at *L1*(1,1) (Fig. 4c) was sequentially paced by stimulator electrodes located at *L4*(1,4), *L4*(4,4) and *L4*(4,1). Following stimulation to lock the AP pace-maker foci to a given stimulator origin, the recorded 3D AP maps plotted as latency maps (Fig. 4d–f) demonstrate clearly that the AP propagation directions are rotated sequentially 90 degrees at each step. These results provide proof-of-concept for spatiotemporal manipulation together with real-time 3D interrogation of propagating APs, and thus offer the potential for sophisticated modulation of cardiac tissue electrophysiology compared to conventional stimulators[29].

The results presented here open up high temporal resolution 3D electrophysiology mapping and manipulation in engineered cardiac tissues, and have potential for impacting several areas of cardiac research including *in vitro* models for drug-screening[6–8] and *in vivo* implants to replace diseased or damaged tissues[10, 11]. In this latter context, we envision our nanoelectronics-cardiac tissue to be surgically-implanted with the input/output wiring (from the scaffold) allowing for continuous monitoring and stimulation of the implanted tissue. Alternatively, it might be interesting to consider syringe co-injection of both nanoelectronic scaffolds[30] and cardiac progenitor cells or stem cells[31] directly into damaged tissues for “smart” repairing with integrated self-monitoring and self-regulation functionality.

More generally, the successful miniaturization of the nanoelectronic scaffolds, which allows matching the size and mechanical properties to conventional passive tissues scaffolds, and the incorporation of large numbers of addressable nanoelectronic devices, which allows 3D mapping, can enable facile integration in a range of engineered tissues for drug screening models through regenerative medicine broadly defined[32]. For example, utilizing softer nanoelectronic and auxiliary scaffolds we could extend the application to engineered 3D neuronal tissues[19]. Rolling the tissue-scaffold-mimicking nanoelectronics into tubular structure could also allow engineering blood vessels[19], and separating distinct cell layers with nanolectronic scaffold layers could be used to study blood brain barrier[33, 34] tissue models in unique ways. Last, we believe it will be important to extend the functionality of the nanoelectronic scaffolds in the future by integrating chemical sensors[35], pressure sensors[36, 37], light-emitting-devices[38] and active matrix addressing[39] since these could expand substantially the capabilities for monitoring and stimulation.

Online Methods

Nanowire synthesis

The Si nanowires (average length of 30 μm) were synthesized on a SiO_2/Si substrate (p-type Si, 0.005 Ω cm, 600 nm oxide, Nova Electronic Materials, LLC., Flower Mound, TX) by a gold nanoparticle-catalyzed vapor-liquid-solid growth method.

Fabrication of free-standing nanoelectronic mesh scaffolds

The 2D free-standing macroporous nanoelectronic mesh scaffolds were fabricated on the oxide surface of SiO_2/Si substrates before being released from the substrate. Key steps used in the fabrication were as follows: (1) 100 nm thick nickel relief film was deposited on substrate by thermal evaporation using PL. (2) A 350 nm layer of SU-8 photoresist (2000.5; MicroChem Corporation, Newton, MA) was spin coated over the entire substrate, followed by a UV exposure to define an array of rectangular pads. (3) The Si nanowires were transferred onto the target Si wafer with selectively patterned SU-8 layer using lubricant-assisted contact printing method. Nanowires arrays were selectively transferred on the pre-defined SU-8 pad arrays. (4) PL was used to pattern the mesh-like bottom SU-8 layer, connecting the pre-defined SU-8 pad arrays with nanowires, that serves as passivating and supporting layer. (5) PL was used to pattern symmetrical Cr/Pd/Cr (1.5/50/1.5 nm) metal S/D contacts followed by thermal evaporation and sequential liftoff process, forming Si nanowire FET sensor arrays on SU-8 meshes. (6) Another top SU-8 passivation layer was patterned using PL. In addition, four circular palladium/platinum electrodes (50/50 nm) were integrated into the nanoelectronic mesh scaffolds as electrical stimulators at four corners in the layer 4 (Fig. 4a). (See more details in Supplementary Methods)

Folding nanoelectronic mesh structures into 3D scaffolds

Free-standing nanoelectronic mesh with Si nanowire FETs were released from the Si wafer by etching the 100 nm nickel relief layer (Nickel Etchant TFB, Transene Company, Inc., Danvers). The nanoelectronic mesh was rinsed with DI water and stored in DI water. The free-standing nanoelectronic mesh scaffolds were folded into a multi-layer structure, with alignment assisted by optical microscope. In order to control a larger separation distance between different mesh layers, a 50 μm thick PLGA electro-spun fiber film was placed in between each mesh layer during folding step. The aligned and folded mesh scaffolds were fixed by Kwik-Sil silicone adhesive (World Precision Instruments, Inc., Sarasota, FL) at boundaries after each folding step. (See more details in Supplementary Methods)

Synthetic nanoelectronics-innervated cardiac tissues

Prior to cell plating, the nanoelectronic mesh scaffolds were thoroughly immersed in 0.5% fibronectin (F1141, Sigma-Aldrich Corporation, Atlanta, GA)/0.02% gelatin (Fisher Scientific, Pittsburgh, PA) solution for 2 h for surface modification. Primary neonatal rat cardiomyocytes were prepared according to previously published procedures[17, 19]. In brief, intact ventricles were isolated from 1–3 day old Sprague/Dawley rats and were then digested at 37 °C in Hanks' balanced salt solution containing collagenase (class II, Worthington Biochemical Corporation, Lakewood, NJ). Isolated cells were purified through pre-plating in

a flask for 2 h to reduce the percentage of non-cardiomyocyte cells. Then the collected cells were concentrated and plated at a cell density of 3–6 × 10^6/cm^2. (See more details in Supplementary Methods).

Electrophysiology measurements

All the electrophysiology measurements were carried out at 37 °C (TC-344D temperature controller, Warner Instruments Corporation) and in Tyrode solution (Sigma-Aldrich Corporation, Atlanta, GA). The conductance of Si nanowire FETs was measured with DC bias set to 100 mV. The drain current was amplified with 16 channel preamplifier (SIM918 Precision current preamplifier, Stanford Research System) and the output data were band pass filtered (0–6000 Hz, home-built system) and recorded at an acquisition rate of 20–100 kHz using a 16-channel A/D converter (Digidata 1440A; Molecular Devices, Sunnyvale, CA) interfaced with a computer running pClamp electrophysiology software (ver. 10.2, Molecular Devices, Axon Laboratory, Sunnyvale, CA). Data analysis was carried out using OriginPro (ver. 8.1, Origin Lab Corp.) and Matlab (ver. R2011a, Mathworks).

Supplementary Material

Refer to Web version on PubMed Central for supplementary material.

Acknowledgments

The authors thank R. Liao and D. Zhang for the inspiring discussion on cardiac electrophysiology and tissue engineering. The authors thank J. L. Huang for the assistance on instrumentation. This work was supported by National Institutes of Health Director’s Pioneer and National Security Science and Engineering Faculty Fellow awards (to C. M. L.).

References

1. Langer R, Vacanti JP. Tissue Engineering. Science. 1993; 260:920–926. [PubMed: 8493529]
2. Eschenhagen T, Zimmermann WH. Engineering myocardial tissue. Circ Res. 2005; 97:1220–1231. [PubMed: 16339494]
3. Shimizu T, et al. Fabrication of pulsatile cardiac tissue grafts using a novel 3-dimensional cell sheet manipulation technique and temperature-responsive cell culture surfaces. Circ Res. 2002; 90:e40. [PubMed: 11861428]
4. Dvir T, Timko BP, Kohane DS, Langer R. Nanotechnological strategies for engineering complex tissues. Nat Nanotechnol. 2011; 6:13–22. [PubMed: 21151110]
5. Papadaki M, et al. Tissue engineering of functional cardiac muscle: molecular, structural, and electrophysiological studies. Am J Physiol-Heart C. 2001; 280:168–178.
6. Hansen A, et al. Development of a Drug Screening Platform Based on Engineered Heart Tissue. Circ Res. 2010; 107:35–44. [PubMed: 20448218]
7. Grosberg A, Alford PW, McCain ML, Parker KK. Ensembles of engineered cardiac tissues for physiological and pharmacological study: Heart on a chip. Lab Chip. 2011; 11:4165–4173. [PubMed: 22072288]
8. Natarajan A, et al. Patterned cardiomyocytes on microelectrode arrays as a functional, high information content drug screening platform. Biomaterials. 2011; 32:4267–4274. [PubMed: 21453966]
9. Griffith LG, Naughton G. Tissue engineering-current challenges and expanding opportunities. Science. 2002:1009–1014. [PubMed: 11834815]

10. Furuta A, et al. Pulsatile cardiac tissue grafts using a novel three-dimensional cell sheet manipulation technique functionally integrates with the host heart, in vivo. Circ Res. 2006; 98:705–712. [PubMed: 16469955]
11. Zimmermann WH, et al. Engineered heart tissue grafts improve systolic and diastolic function in infarcted rat hearts. Nat Med. 2006; 12:452–458. [PubMed: 16582915]
12. St-Pierre F, et al. High-fidelity optical reporting of neuronal electrical activity with an ultrafast fluorescent voltage sensor. Nat Neurosci. 2014; 17:884–889. [PubMed: 24755780]
13. Herron TJ, Lee P, Jalife J. Optical Imaging of Voltage and Calcium in Cardiac Cells & Tissues. Circ Res. 2012; 110:609–623. [PubMed: 22343556]
14. Kralj JM, Douglass AD, Hochbaum DR, Maclaurin D, Cohen AE. Optical recording of action potentials in mammalian neurons using a microbial rhodopsin. Nat Methods. 2012; 9:90–95. [PubMed: 22120467]
15. Huisken J, Swoger J, Del Bene F, Wittbrodt J, Stelzer EHK. Optical sectioning deep inside live embryos by selective plane illumination microscopy. Science. 2004; 305:1007–1009. [PubMed: 15310904]
16. Kim DH, et al. Materials for multifunctional balloon catheters with capabilities in cardiac electrophysiological mapping and ablation therapy. Nat Mater. 2011; 10:316–323. [PubMed: 21378969]
17. Cohen-Karni T, Timko BP, Weiss LE, Lieber CM. Flexible electrical recording from cells using nanowire transistor arrays. P Natl Acad Sci USA. 2009; 106:7309–7313.
18. Viventi J, et al. A Conformal, Bio-Interfaced Class of Silicon Electronics for Mapping Cardiac Electrophysiology. Sci Transl Med. 2010; 2:24ra22.
19. Tian BZ, et al. Macroporous nanowire nanoelectronic scaffolds for synthetic tissues. Nat Mater. 2012; 11:986–994. [PubMed: 22922448]
20. Place ES, George JH, Williams CK, Stevens MM. Synthetic polymer scaffolds for tissue engineering. Chem Soc Rev. 2009; 38:1139–1151. [PubMed: 19421585]
21. Zhang D, et al. Tissue-engineered cardiac patch for advanced functional maturation of human ESC-derived cardiomyocytes. Biomaterials. 2013; 34:5813–5820. [PubMed: 23642535]
22. Yelbuz TM, Choma MA, Thrane L, Kirby ML, Izatt JA. Optical coherence tomography - A new high-resolution imaging technology to study cardiac development in chick embryos. Circulation. 2002; 106:2771–2774. [PubMed: 12451001]
23. Miragoli M, Gaudesius G, Rohr S. Electrotonic modulation of cardiac impulse conduction by myofibroblasts. Circ Res. 2006; 98:801–810. [PubMed: 16484613]
24. Khademhosseini A, et al. Microfluidic patterning for fabrication of contractile cardiac organoids. Biomedical microdevices. 2007; 9:149–157. [PubMed: 17146728]
25. Timko BP, Cohen-Karni T, Qing Q, Tian B, Lieber CM. Design and Implementation of Functional Nanoelectronic Interfaces With Biomolecules, Cells, and Tissue Using Nanowire Device Arrays. IEEE Trans Nanotechnol. 2010; 9:269–280. [PubMed: 21785576]
26. Zhang JH, et al. Functional Cardiomyocytes Derived From Human Induced Pluripotent Stem Cells. Circ Res. 2009; 104:e30. [PubMed: 19213953]
27. Laflamme MA, et al. Cardiomyocytes derived from human embryonic stem cells in pro-survival factors enhance function of infarcted rat hearts. Nat Biotechnol. 2007; 25:1015–1024. [PubMed: 17721512]
28. Myles RC, Wang LG, Kang CY, Bers DM, Ripplinger CM. Local beta-Adrenergic Stimulation Overcomes Source-Sink Mismatch to Generate Focal Arrhythmia. Circ Res. 2012; 110:1454–1464. [PubMed: 22539768]
29. Iravanian S, et al. Functional reentry in cultured monolayers of neonatal rat cardiac cells. Am J Physiol-Heart C. 2003; 285:449–456.
30. Liu J, et al. Syringe-injectable electronics. Nat Nanotechnol. 2015; 10:629–636. [PubMed: 26053995]
31. Garbern JC, Lee RT. Cardiac stem cell therapy and the promise of heart regeneration. Cell Stem Cell. 2013; 12:689–698. [PubMed: 23746978]

32. Wobma H, Vunjak-Novakovic G. Tissue Engineering and Regenerative Medicine 2015: A Year in Review. Tissue engineering. Part B, Reviews. 2016; 22:101–113. [PubMed: 26714410]
33. Wong AD, et al. The blood-brain barrier: an engineering perspective. Frontiers in neuroengineering. 2013; 6:7. [PubMed: 24009582]
34. Wang XY, et al. Engineering interconnected 3D vascular networks in hydrogels using molded sodium alginate lattice as the sacrificial template. Lab Chip. 2014; 14:2709–2716. [PubMed: 24887141]
35. McAlpine MC, Ahmad H, Wang DW, Heath JR. Highly ordered nanowire arrays on plastic substrates for ultrasensitive flexible chemical sensors. Nat Mater. 2007; 6:379–384. [PubMed: 17450146]
36. Annabi N, et al. Hydrogel-coated microfluidic channels for cardiomyocyte culture. Lab Chip. 2013; 13:3569–3577. [PubMed: 23728018]
37. Wang C, et al. User-interactive electronic skin for instantaneous pressure visualization. Nat Mater. 2013; 12:899–904. [PubMed: 23872732]
38. Huang Y, Duan X, Lieber CM. Nanowires for integrated multicolor nanophotonics. Small. 2005; 1:142–147. [PubMed: 17193365]
39. Takei K, et al. Nanowire active-matrix circuitry for low-voltage macroscale artificial skin. Nat Mater. 2010; 9:821–826. [PubMed: 20835235]

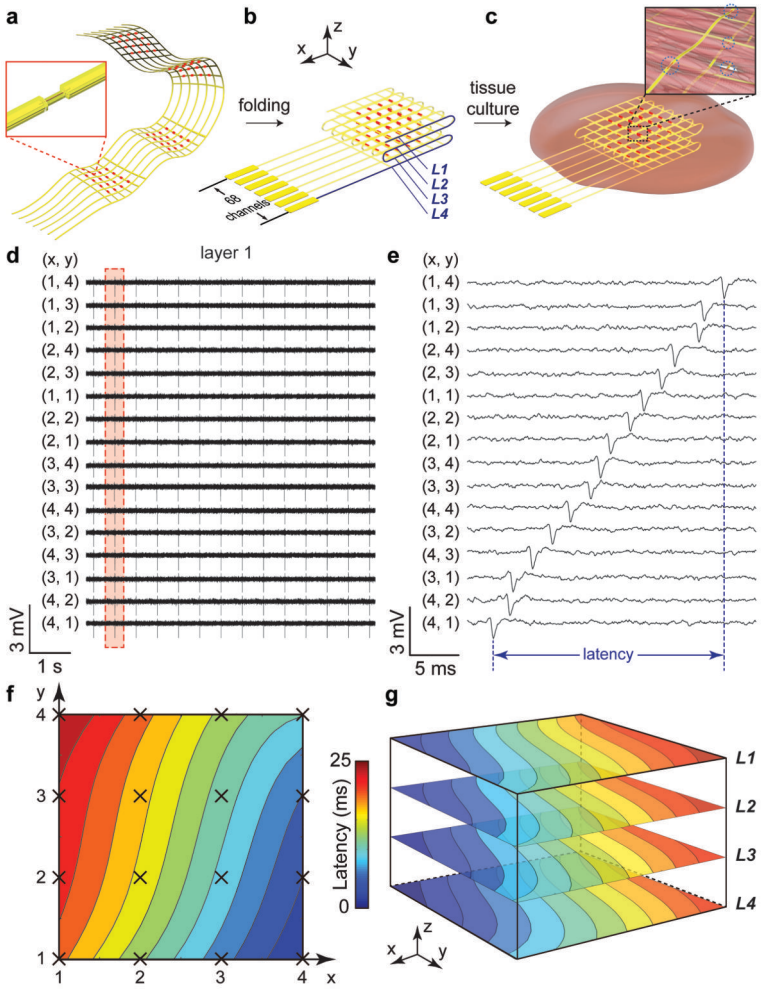

Figure 1. 3D spatiotemporal mapping of APs

(**a**) Schematic of free-standing macroporous nanoelectronic scaffold with nanowire FET arrays (red dots); inset, one nanowire FET. In (**a**–**c**), a limited number of input/output leads are shown for clarity; the total for the design as indicated in (**b**) is 68. (**b**) Folded 3D free-standing scaffolds with four layers of individually addressable FET sensors. (**c**) Schematic of nanoelectronic scaffold/cardiac tissue resulting from culture of cardiac cells within the 3D folded scaffold; inset, nanoelectronic sensors (blue circles) innervate the 3D cell network. (**d**) Simultaneous traces recorded from 16 sensors in the top layer (*L1*) from nanoelectronics-cardiac tissue. The (x,y) coordinates of each element from the 4 × 4 array are shown. (**e**) Zoom-in view of a single AP spike recorded from each device during the time indicated by the dashed-box in (**d**). The time latency between APs recorded from different devices is evident and specifically indicated for FETs (4,1) to (1,4). (**f**) Isochronal map of time latency in *L1*; mapping area is ca. 25 mm^2. (**g**) 3D isochronal map of time latency through the sample, where *L1*–*L4* correspond to the four layers of 4 × 4 device arrays innervating the cardiac tissue. Mapping area is ca. 25 mm^2 × 200 μm.

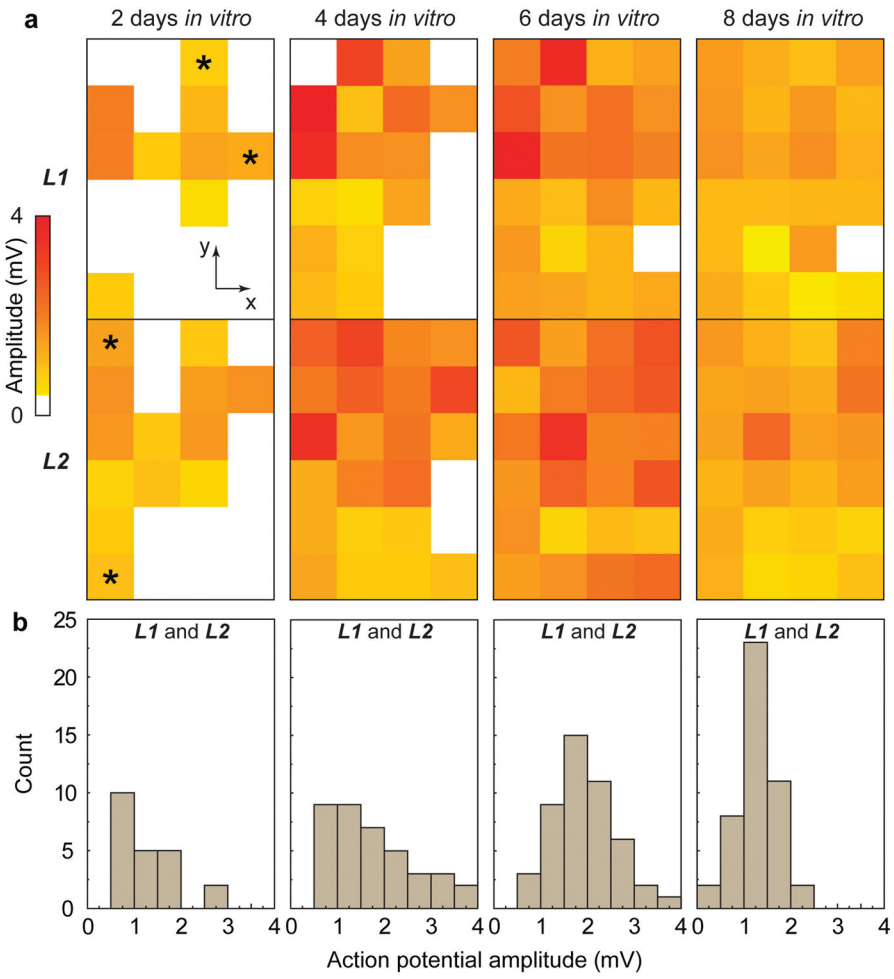

Figure 2. AP evolution during tissue development

(**a**) Amplitudes of spontaneous extracellular APs recorded from 4 × 6 nanowire FET arrays in two layers at 2, 4, 6 and 8 DIV. White squares correspond to coordinates where extracellular APs are absent or below the detection limit (1× standard deviation of noise level). Time-dependent data recorded from four devices (2 × *L1* and 2 × *L2*) indicated with asterisks at 2 DIV are shown in Supplementary Fig. 5. (**b**) Histogram of extracellular AP amplitudes recorded from the 3D nanoelectronics-cardiac tissue sample at 2, 4, 6 and 8 DIV.

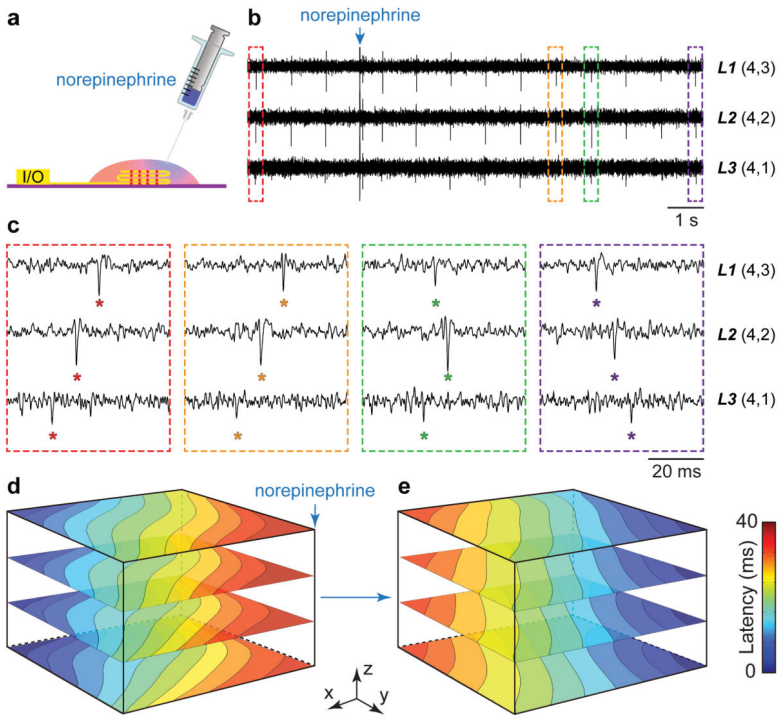

Figure 3. Arrhythmia induced by localized norepinephrine injection

(**a**) Schematic of measurement setup highlighting the syringe injection of norepinephrine at a localized spot on the 3D nanoelectronics-cardiac tissue. (**b**) Time-dependent traces from three sensors in *L1*, *L2*, *L3* with synchronized and periodic APs. Blue arrow indicates the injection time point of ~25 μL norepinephrine at concentration of 100 μM. (**c**) Zoom-in view of the four dashed-box regions in (**b**) depicting time latency between APs before and 5–10 s after norepinephrine addition. (**d**–**e**) 3D isochronal time latency maps before (**d**) and 5 min after (**e**) local norepinephrine injection; blue arrow in (**d**) indicates injection position.

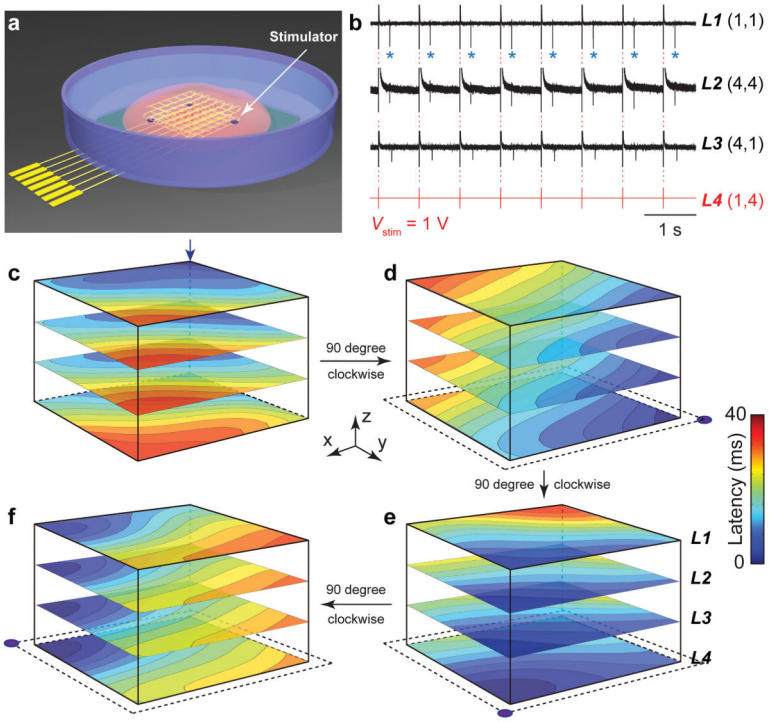

Figure 4. Active spatiotemporal regulation of APs

(**a**) Schematic illustrating positions of individually addressable stimulator electrodes (purple dots) in the nanoelectronic scaffold. (**b**) Time-dependent traces recorded from nanowire FETs in layers *L1*, *L2*, *L3* under periodic biphasic stimulation spike train in *L4*. Stimulation peak width, amplitude and frequency were 1 ms, 1 V and 1.25 Hz, respectively. Blue asterisks in *L1* trace highlight APs (downward spikes) versus capacitive coupling peaks (red dashed-lines). (**c**–**f**) 3D isochronal time latency maps for original pace-maker foci location (**c**, blue arrow), and sequential 90 degree rotations of the AP propagation direction using the indicated simulator electrodes (lower corners panels **d** to **f**).